

# Searching for CU Vir-type cyclotron maser from $\sigma$ Ori E: The role of the magnetic quadrupole component

P. Leto<sup>1</sup> \*, C. Trigilio<sup>1</sup>, C. S. Buemi<sup>1</sup>, F. Leone<sup>2</sup>, G. Umana<sup>1</sup>

<sup>1</sup>INAF - Osservatorio Astrofisico di Catania, Via S. Sofia 78, 95123 Catania, Italy

<sup>2</sup>Università di Catania, Dipartimento di Fisica e Astronomia, Sezione Astrofisica, Via S. Sofia 78, 95123 Catania, Italy

## ABSTRACT

In this paper we present new and archive radio measurements obtained with the Very Large Array of the magnetic chemically peculiar (MCP) star  $\sigma$  Ori E. The radio data have been obtained at different frequencies and are well distributed along the rotational phases. We analyze in detail the radio emission from  $\sigma$  Ori E with the aim to search evidence of circularly polarized radio pulses. Up to now, among the MCP stars only CU Virginis shows 100% polarized time-stable radio pulses, explained as highly directive electron cyclotron maser emission, visible from Earth at particular rotational phases, like a pulsar. Our analysis shows that there is no hint of coherent emission at frequencies below 15 GHz. We conclude that the presence of a quadrupolar component of the magnetic field, dominant within few stellar radii from the star, where the maser emission should be generated, inhibits the onset of the cyclotron maser instability in  $\sigma$  Ori E.

**Key words:** masers – stars: chemically peculiar – stars: individual:  $\sigma$  Ori E – stars: magnetic field – radio continuum: stars.

## 1 INTRODUCTION

Magnetic chemically peculiar (MCP) stars present photometric, spectroscopic and magnetic variability with a single period. As to the magnetic field, the most important observable is the effective or longitudinal magnetic field ( $B_e$ ), that is the average over the stellar visible disk of the longitudinal components of the magnetic field (Leone, Catalano & Catanzaro 2000). To explain the previous phenomenology Babcock (1949) and Stibbs (1950) proposed the presence of a magnetic dipole, whose axis is tilted with respect to the rotational axis, the so called Oblique Rotator Model, and a non-uniform distribution of some chemical elements on the stellar surface which rotates rigidly. Spectral, light and magnetic variability would be a consequence of stellar rotation. Later, it has been cleared that the MCP stars can present multipolar magnetic fields. Bychkov, Bychkova & Madej (2005) collect all available MCP magnetic curves and they show that in many cases their shape is more complex than a simple sinusoidal wave.

Non-thermal radio emission is observed from about 25% of the MCP stars (Leone, Trigilio & Umana 1994). In accord with the oblique rotator model, the radio emission is also variable as a consequence of the stellar rotation (Leone 1991), suggesting that the radio emission arises from a stable

optically thick co-rotating magnetosphere. Radio emission is ascribed to a radiatively-driven stellar wind. The gas flow brakes the magnetic field lines far from the star (Alfvén surface) forming current sheets, where electrons are accelerated to the mildly relativistic regime. Energetic electrons propagate back, along thin magnetospheric layers named middle magnetosphere, to the inner magnetospheric regions radiating by gyrosynchrotron emission mechanism at the radio wavelengths (Trigilio et al. 2004; Leto et al. 2006).

Out of MCP stars, CU Virginis (HD 124224 = HR 5313) is the only known source characterized by broadband, highly polarized and time-stable pulses at 1.4 and 2.5 GHz (Trigilio et al. 2000, 2008, 2011; Ravi et al. 2010; Lo et al. 2012). Stevens & George (2010) have also reported a pulse detection at 610 MHz. Radio pulses stand out for 1 dex over the continuous emission, the single pulse duration ranges from 5 to 10% of the rotational period and are observed in coincidence with the null values of  $B_e$ , that is when the magnetic dipole axis is perpendicular to the line of sight.

Such a behavior has been ascribed to the electron cyclotron maser (ECM) emission mechanism powered by an anisotropic pitch-angle (angle between electron velocity and local magnetic field) distribution that the non-thermal electrons, responsible of the gyrosynchrotron stellar radio emission, can develop propagating in a magnetic flux tube towards regions of increasing magnetic field strength. Electrons with an initial large pitch-angle are soon reflected outward due to the magnetic mirroring, whereas electrons with

\* E-mail: pleto@oact.inaf.it

a small pitch angle can reach the inner magnetospheric layers where they are thermalized in the dense plasma. The reflected electron population is characterized by a pitch angle distribution deprived by the electrons with a small pitch angle. This mechanism amplifies the extraordinary magneto-ionic mode producing nearly 100% circularly polarized radiation at frequencies very close to the first or second harmonic of the local gyro-frequency ( $\nu_B = 2.8 \times 10^{-3} B/G$  GHz), in a direction almost perpendicular to the local magnetic field lines (Melrose & Dulk 1982). However the fundamental harmonic is probably suppressed by the gyromagnetic absorption.

The ECM mechanism has been considered to account for the strongly polarized, intense and narrow band short time spikes observed in the Sun (Willson 1985; Winglee & Dulk 1986), dMe flare stars (Lang et al. 1983; Lang & Willson 1988; Abada-Simon et al. 1994, 1997) and RS CVn binaries (Slee, Haynes & Wright 1984; Osten et al. 2004). ECM explains the planetary low frequency emission, in particular the Jupiter decametric radiation and the Earth's Auroral Kilometric Radiation (AKR) (Treumann 2006).

The fully polarized pulses observed on CU Vir are broadband and persistent over long timescale (years). The large bandwidth is a consequence of the wide range of the magnetic field strength in the region where the maser amplification occurs. The observed maser emission is the superimposition of narrowband emission from different rings above the magnetic poles. The continuous supply of non-thermal electrons, developing a loss-cone anisotropy, maintains stable the electron cyclotron maser emission. Following the tangent plane beaming model, proposed for the AKR (Mutel, Christopher & Pickett 2008) and successfully applied to explain the narrow peaks observed on CU Vir (Trigilio et al. 2011), the amplified radiation is beamed tangentially to the polar ring where the cyclotron maser instability takes place. Then, during the propagation through the denser magnetized plasma of the inner magnetosphere, the radiation is refracted upward by a few degrees (Trigilio et al. 2011; Lo et al. 2012). Since the magnitude of this angle depends on frequency, the radiation is detected in different moments during the rotation of the star, causing a frequency drift of the observed pulses.

Highly polarized broad-band radio pulses, still explained as ECM, have been also recognized in the ultra cool main sequence dwarf stars (Berger et al. 2001; Burgasser & Putman 2005; Hallinan et al. 2006, 2007, 2008). Despite the great difference of the physical characteristics between these two extreme classes of stars, late M and MCP stars show similar behavior at the radio wavelengths. The existence of a well ordered and stable axisymmetric magnetic field in the rapidly rotating fully convective M type stars (Donati et al. 2006a, 2008; Morin et al. 2008a,b) can be the reason of the observed similarity.

The study of the radio pulses from CU Vir also provided the possibility to evidence variations of the stellar rotational period with a high degree of confidence (Trigilio et al. 2008, 2011). Discovering the CU Virginis type coherent emission in other MCP stars would provide an useful tool for the study of the angular momentum evolution in this kind of stars.

On the basis of the results gathered from CU Vir, the possibility to observe the same type of coherent emission

from other MCP stars requires an appropriate stellar magnetic field geometry, with  $B_e$  presenting at least a null value during the stellar rotation. Among the already known MCP stars presenting radio emission  $\sigma$  Ori E (HD 37479 = HR 1932) is an ideal candidate to search for the presence of this type of coherent emission. Its magnetic field presents the appropriate geometry, being the rotation axis inclination  $i = 72^\circ$  and magnetic axis obliquity  $\beta = 56^\circ$  (Bohlender et al. 1987).

The coherent pulses have been observed from CU Vir ( $B_p = 3000$  G, Trigilio et al. (2000)) at low frequencies ( $< 2.5$  GHz). We expect that ECM emission from  $\sigma$  Ori E could be observed at higher frequencies, as a consequence of the stronger magnetic field ( $B_p = 6800$  G, Trigilio et al. (2004)). In this paper we present new multifrequency (1.4, 5, 8.4, 15, 22 and 43 GHz) VLA observations of  $\sigma$  Ori E. In addition, to obtain as complete as possible radio light-curves, we have retrieved all unpublished VLA archive data. The primary aim is to search for amplified emission strongly polarized, but we can also probe different layers of the  $\sigma$  Ori E magnetosphere, because of the dependence of the frequency of the gyrosynchrotron radio emission from the magnetic field strength.

## 2 $\sigma$ ORIE

$\sigma$  Ori E is a magnetic helium-strong star of spectral type B2V, mass  $M_* = 8.9 M_\odot$  (Hunger, Heber & Groote 1989), radius  $R_* = 4.2 R_\odot$  (Shore & Brown 1990), located at a distance of about 350 pc (ESA 1997). It is significantly hotter than CU Vir (spectral type A0V), this involves a stronger radiatively driven wind and, therefore, a greater mass loss rate. On the other hand, the polar magnetic field strength of  $\sigma$  Ori E is 6800 G, versus 3000 G of CU Vir, and the rotational period is 1.19<sup>d</sup>, versus 0.52<sup>d</sup>. All these two factors influence the confinement of the wind, resulting that the two stars have similar magnetospheres, both with Alfvén radius about 15  $R_*$  (Trigilio et al. 2004; Leto et al. 2006). This reinforces our decision to search evidence of CU Vir-type coherent emission from  $\sigma$  Ori E.

The long history of the photometric, spectroscopic and magnetic variability presented by  $\sigma$  Ori E is documented in the *Catalog of observed periods for the AP stars* by Catalano & Renson (1984) and its supplements (Catalano & Renson 1988; Catalano, Renson & Leone 1991, 1993). Townsend et al. (2010) have concluded that  $\sigma$  Ori E is spinning down because of the magnetic braking and supplied the ephemeris:

$$\text{HJD} = 2442778.829 + 1.1908229E + 1.44 \times 10^{-9} E^2 \quad [\text{days}]$$

referred to the deeper light minimum. The spin down of  $\sigma$  Ori E was already theoretically predicted by magnetohydrodynamics simulations (Ud-Doula, Owocky & Townsend 2009).

The global magnetic field of  $\sigma$  Ori E is steady over three decades (Oksala et al. 2011) and since Landstreet & Borra (1978) a pure magnetic dipole is assumed. Fig. 1 shows the magnetic field measurements of  $\sigma$  Ori E by Landstreet & Borra (1978), Bohlender et al. (1987) and

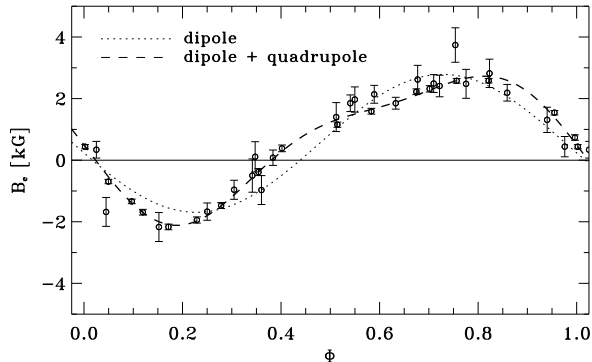


**Figure 1.** Fit of the literature magnetic field measurements – open circles. Legend of line style: single wave fit – dot line, double wave fit – dashed line. The solid horizontal line coincides with the null effective surface magnetic field.

Oksala et al. (2011) phased with the previous ephemeris. A data fit with a single wave equation:

$$B_e = B_0 + B_1 \sin 2\pi(\Phi - \Phi_0)$$

gives a reduced  $\chi^2 = 12.4$ . Here  $B_0 = 0.55 \pm 0.02$  [kG],  $B_1 = 2.24 \pm 0.03$  [kG] and  $\Phi_0 = 0.478 \pm 0.002$ .

From long time it is known that the variability of MCP stars can be accurately modeled through a sinusoidal wave and its first harmonic (Catalano, Kroll & Leone 1991). Indeed a fit of magnetic data with the equation:

$$B_e = B_0 + B_1 \sin 2\pi(\Phi - \Phi_0) + B_2 \sin 2\pi(2\Phi - \Phi_1)$$

results in a reduced  $\chi^2 = 1.6$ , suggesting the non-dipolar nature of the  $\sigma$  Ori E magnetic field. Here  $B_0 = 0.62 \pm 0.02$  [kG],  $B_1 = 2.21 \pm 0.03$  [kG],  $B_2 = 0.63 \pm 0.03$  [kG],  $\Phi_0 = 0.473 \pm 0.002$  and  $\Phi_1 = 0.563 \pm 0.007$ .

Landolfi, Bagnulo & Landi Degl’Innocenti (1998) shown that the  $B_e$  variation due to a pure quadrupole is about 10% of the variability due to a dipole of equal polar strength. This means that  $\sigma$  Ori E would present a quadrupole component at least two times stronger than the dipole one.

The presence of multipolar magnetic components in  $\sigma$  Ori E is testified by the asymmetric emission features on the  $H\alpha$  wings. These periodically variable features have been ascribed to two circumstellar plasma clouds trapped in the magnetosphere and co-rotating with the star (Landstreet & Borra 1978); trapped material was also recognized from UV observations (Smith & Groote 2001). To explain why one of the two feature is stronger than the other, Groote & Hunger (1982) suggested an asymmetry in the two clouds. In the case of  $\delta$  Ori C, an MCP star twin of  $\sigma$  Ori E, also presenting similar asymmetric emission features on the  $H\alpha$  wings, Leone et al. (2010) mapped the circumstellar matter distribution and ascribed the asymmetry between the two clouds to the magnetic quadrupole component necessary to explain the Stokes V profiles of the spectral lines.

We conclude that the  $\sigma$  Ori E phenomenology cannot be modeled as a simple dipole and that higher order components are necessary to explain the observational data.

**Table 1.** VLA observing log.

Code	Frequencies [GHz]	Epoch	conf.	Flux cal	Phase cal
AL346	5/15/43	95-Apr	D	3C48	0541–056
AT233	1.4/5	99-Oct	AB	3C48	0541–056
AL568	8.4/15	02-May	AB	3C286	0541–056
AL618	5/15/22/43	04-Jan	BC	3C286	0541–056
Archive VLA data					
AL267	5/8.4/15	92-Oct	A	3C286	0541–056
AL348	5/8.4/15/22/43	95-Mar	D	3C286	0532+075
AL372	5/8.4/15	96-Mar	C	3C48	0541–056

### 3 RADIO OBSERVATIONS AND DATA REDUCTION

Multi-frequency observations of  $\sigma$  Ori E were carried out with the VLA<sup>1</sup> in different epochs. Table 1 reports the instrumental and observational details for each data set.

To avoid significative phase fluctuations, scans on  $\sigma$  Ori E were shorter than the Earth atmosphere coherence time and embedded between phase calibrator measurements. The 22 and 43 GHz observations were carried out using the fast switching mode between source and phase calibrator.

The data were calibrated and mapped using the standard procedures of the Astronomical Image Processing System (AIPS). The flux density for the Stokes I parameter was obtained by fitting a two-dimensional gaussian (JMFIT) at the source position in the cleaned maps integrated over contiguous scans, the integration time ranges from about 10 minutes to about 1 hour. As the uncertainty in the flux density measurements we assume the r.m.s. of the map.

The fraction of the circularly polarized flux density (Stokes V parameter) was instead determined performing the direct Fourier transform of the visibilities at the source position (DFTPL) without any temporal average. We are justified in this procedure by the absence of other circularly polarized sources in the field. Stokes V were later averaged with the same integration time of Stokes I. All VLA measurements are listed in Table 2.

### 4 RADIO PROPERTIES OF $\sigma$ ORIE

#### 4.1 Light curves

Fig. 2 shows the radio flux versus the rotational phase for  $\nu \leq 15$  GHz. For completeness, we plot also the literature measurements at 5 GHz by Drake et al. (1987) and Leone & Umana (1993). The top panel shows the variability of  $B_e$  (Oksala et al. 2011; Landstreet & Borra 1978; Bohlender et al. 1987).

As already known (Leone 1991; Leone & Umana 1993; Triglio et al. 2004) the light curve at 5 GHz of  $\sigma$  Ori E is characterized by the presence of two maxima associated

<sup>1</sup> The Very Large Array is a facility of the National Radio Astronomy Observatory which is operated by Associated Universities, Inc. under cooperative agreement with the National Science Foundation.

**Table 2.** New and archival VLA observations.

JD	S <sub>I</sub> (S <sub>V</sub> )	σ	JD	S <sub>I</sub> (S <sub>V</sub> )	σ	JD	S <sub>I</sub> (S <sub>V</sub> )	σ	JD	S <sub>I</sub> (S <sub>V</sub> )	σ	JD	S <sub>I</sub> (S <sub>V</sub> )	σ
2400000+	mJy	mJy	2400000+	mJy	mJy	2400000+	mJy	mJy	2400000+	mJy	mJy	2400000+	mJy	mJy
<b>ν=1.4 GHz</b>			50171.677 <sup>d</sup>	4.10(−0.03)	0.07	51461.958 <sup>e</sup>	4.42(+0.13)	0.05	50171.629 <sup>d</sup>	3.78(−0.27)	0.05	49827.591 <sup>c</sup>	4.50(+0.10)	0.40
51453.833 <sup>e</sup>	2.60(+0.10)	0.15	50172.377 <sup>d</sup>	4.10(+0.30)	0.10	51461.982 <sup>e</sup>	4.14(+0.20)	0.06	50171.688 <sup>d</sup>	4.27(−0.14)	0.06	49833.434 <sup>c</sup>	3.30(−0.40)	0.30
51453.862 <sup>e</sup>	2.50(+0.10)	0.15	50172.437 <sup>d</sup>	3.43(+0.22)	0.08	51462.009 <sup>e</sup>	4.14(+0.15)	0.06	50172.448 <sup>d</sup>	3.38(+0.43)	0.06	49837.382 <sup>c</sup>	4.10(+0.10)	0.30
51453.896 <sup>e</sup>	2.10(+0.00)	0.15	50172.496 <sup>d</sup>	3.14(+0.05)	0.08	51462.037 <sup>e</sup>	4.21(+0.35)	0.06	50172.507 <sup>d</sup>	3.23(+0.29)	0.06	50170.358 <sup>d</sup>	3.20(−0.30)	0.10
51453.951 <sup>e</sup>	2.00(+0.00)	0.20	50172.555 <sup>d</sup>	3.44(+0.04)	0.08	51462.061 <sup>e</sup>	4.00(+0.24)	0.05	50172.567 <sup>d</sup>	3.99(+0.10)	0.05	50170.418 <sup>d</sup>	3.40(−0.30)	0.10
51453.998 <sup>e</sup>	1.70(+0.10)	0.20	50172.615 <sup>d</sup>	3.31(−0.01)	0.07	51462.085 <sup>e</sup>	3.88(+0.15)	0.06	50172.626 <sup>d</sup>	4.27(+0.05)	0.05	50170.477 <sup>d</sup>	3.10(−0.30)	0.10
51454.050 <sup>e</sup>	1.80(−0.10)	0.20	50172.674 <sup>d</sup>	3.44(+0.08)	0.07	51462.111 <sup>e</sup>	3.53(+0.27)	0.05	50172.685 <sup>d</sup>	4.36(+0.04)	0.06	50170.537 <sup>d</sup>	3.80(−0.40)	0.10
51454.135 <sup>e</sup>	2.30(+0.00)	0.20	51453.831 <sup>e</sup>	3.10(+0.10)	0.10	53031.789 <sup>g</sup>	3.40(+0.05)	0.08	52417.192 <sup>f</sup>	3.10(+0.50)	0.20	50170.596 <sup>d</sup>	5.20(−0.40)	0.10
51455.827 <sup>e</sup>	2.00(−0.10)	0.15	51453.855 <sup>e</sup>	3.20(+0.20)	0.20	<b>ν=8.4 GHz</b>			52417.200 <sup>f</sup>	2.80(+0.70)	0.20	50170.655 <sup>d</sup>	5.60(−0.20)	0.10
51455.862 <sup>e</sup>	2.30(+0.10)	0.10	51453.878 <sup>e</sup>	3.10(+0.10)	0.10	48906.869 <sup>a</sup>	4.40(+0.10)	0.10	52417.208 <sup>f</sup>	2.80(+0.30)	0.20	50170.707 <sup>d</sup>	5.80(−0.20)	0.20
51455.902 <sup>e</sup>	2.40(+0.00)	0.10	51453.902 <sup>e</sup>	3.40(+0.10)	0.10	48906.887 <sup>a</sup>	4.40(+0.00)	0.10	52417.217 <sup>f</sup>	3.20(+0.30)	0.20	50171.411 <sup>d</sup>	3.70(+0.20)	0.10
51455.941 <sup>e</sup>	2.80(−0.10)	0.10	51453.934 <sup>e</sup>	3.11(−0.02)	0.08	48906.901 <sup>a</sup>	4.20(−0.30)	0.10	52417.227 <sup>f</sup>	2.80(+0.60)	0.20	50171.470 <sup>d</sup>	4.40(+0.00)	0.10
51455.998 <sup>e</sup>	2.70(+0.10)	0.10	51453.957 <sup>e</sup>	3.09(+0.11)	0.07	48906.915 <sup>a</sup>	4.00(−0.10)	0.10	52417.238 <sup>f</sup>	2.80(+0.30)	0.20	50171.530 <sup>d</sup>	4.10(+0.00)	0.10
51456.067 <sup>e</sup>	2.70(+0.10)	0.10	51453.981 <sup>e</sup>	3.16(+0.13)	0.07	48906.934 <sup>a</sup>	3.90(−0.20)	0.10	52417.250 <sup>f</sup>	2.50(+0.20)	0.20	50171.589 <sup>d</sup>	3.90(−0.30)	0.10
51456.120 <sup>e</sup>	2.70(+0.00)	0.10	51454.004 <sup>e</sup>	3.12(+0.01)	0.06	48907.011 <sup>a</sup>	4.30(−0.20)	0.10	52417.262 <sup>f</sup>	2.50(+0.30)	0.10	50171.648 <sup>d</sup>	5.10(−0.40)	0.10
51456.162 <sup>e</sup>	2.80(+0.00)	0.10	51454.032 <sup>e</sup>	3.25(−0.07)	0.05	48907.038 <sup>a</sup>	4.60(−0.10)	0.10	52417.276 <sup>f</sup>	2.80(+0.20)	0.10	50171.700 <sup>d</sup>	3.90(−0.80)	0.20
51458.841 <sup>e</sup>	2.00(−0.10)	0.08	51454.060 <sup>e</sup>	3.28(−0.05)	0.06	48907.048 <sup>a</sup>	4.70(−0.10)	0.10	52417.291 <sup>f</sup>	3.10(+0.10)	0.10	50172.408 <sup>d</sup>	4.00(+0.80)	0.20
51458.899 <sup>e</sup>	2.20(+0.00)	0.10	51454.083 <sup>e</sup>	3.22(+0.01)	0.06	48907.067 <sup>a</sup>	4.80(+0.00)	0.10	52417.306 <sup>f</sup>	3.60(+0.00)	0.10	50172.467 <sup>d</sup>	3.20(+0.20)	0.20
51458.956 <sup>e</sup>	2.30(−0.06)	0.07	51454.107 <sup>e</sup>	3.44(−0.05)	0.06	48907.086 <sup>a</sup>	4.90(+0.20)	0.10	52417.321 <sup>f</sup>	3.60(−0.20)	0.10	50172.527 <sup>d</sup>	3.20(+0.20)	0.10
51459.031 <sup>e</sup>	2.60(+0.04)	0.08	51454.130 <sup>e</sup>	3.78(+0.00)	0.06	48907.163 <sup>a</sup>	5.00(+0.10)	0.10	52417.337 <sup>f</sup>	3.90(+0.10)	0.10	50172.586 <sup>d</sup>	4.80(−0.10)	0.10
51459.122 <sup>e</sup>	2.40(+0.02)	0.08	51454.154 <sup>e</sup>	3.96(−0.04)	0.07	48908.854 <sup>a</sup>	3.90(+0.20)	0.10	52417.352 <sup>f</sup>	4.00(+0.00)	0.10	50172.645 <sup>d</sup>	5.10(+0.10)	0.10
51461.929 <sup>e</sup>	2.70(+0.00)	0.10	51454.176 <sup>e</sup>	3.87(−0.13)	0.08	48908.873 <sup>a</sup>	3.70(+0.10)	0.10	52417.367 <sup>f</sup>	3.70(−0.10)	0.10	50172.697 <sup>d</sup>	5.80(−0.10)	0.20
51461.976 <sup>e</sup>	2.80(+0.20)	0.10	51455.821 <sup>e</sup>	3.30(+0.20)	0.10	48908.891 <sup>a</sup>	3.50(+0.40)	0.10	52417.383 <sup>f</sup>	3.73(−0.06)	0.08	52417.229 <sup>f</sup>	3.30(+0.70)	0.15
51462.021 <sup>e</sup>	2.80(+0.10)	0.10	51455.845 <sup>e</sup>	3.41(+0.15)	0.08	48908.910 <sup>a</sup>	3.30(+0.20)	0.10	52417.398 <sup>f</sup>	3.70(+0.10)	0.10	52417.284 <sup>f</sup>	2.90(+0.40)	0.20
51462.067 <sup>e</sup>	2.80(+0.00)	0.10	51455.868 <sup>e</sup>	3.75(+0.01)	0.08	48908.929 <sup>a</sup>	3.20(+0.40)	0.10	52417.413 <sup>f</sup>	4.00(−0.10)	0.10	52417.315 <sup>f</sup>	3.20(+0.00)	0.15
<b>ν=5 GHz</b>			51455.892 <sup>e</sup>	3.80(+0.20)	0.10	48909.006 <sup>a</sup>	2.80(+0.20)	0.10	52417.428 <sup>f</sup>	3.90(−0.10)	0.10	52417.345 <sup>f</sup>	3.90(+0.10)	0.15
48906.821 <sup>b</sup>	3.20(+0.00)	0.10	51455.923 <sup>e</sup>	4.03(+0.18)	0.08	48909.024 <sup>a</sup>	2.80(+0.20)	0.10	52417.444 <sup>f</sup>	4.00(+0.00)	0.10	52417.376 <sup>f</sup>	4.50(−0.40)	0.15
48906.973 <sup>b</sup>	4.10(+0.20)	0.10	51455.947 <sup>e</sup>	4.13(+0.14)	0.08	48909.043 <sup>a</sup>	3.00(+0.10)	0.10	52417.459 <sup>f</sup>	4.10(−0.10)	0.10	52417.406 <sup>f</sup>	5.20(+0.50)	0.15
48907.125 <sup>b</sup>	4.90(−0.10)	0.10	51455.971 <sup>e</sup>	4.04(+0.18)	0.07	48909.062 <sup>a</sup>	2.70(+0.20)	0.10	52417.473 <sup>f</sup>	4.00(−0.10)	0.10	52417.437 <sup>f</sup>	5.00(+0.00)	0.15
48908.816 <sup>b</sup>	4.70(+0.20)	0.10	51455.994 <sup>e</sup>	4.09(+0.15)	0.08	48909.081 <sup>a</sup>	3.50(+0.00)	0.10	52417.484 <sup>f</sup>	4.00(+0.00)	0.10	52417.477 <sup>f</sup>	3.90(−0.10)	0.20
48908.968 <sup>b</sup>	3.20(+0.00)	0.10	51456.022 <sup>e</sup>	3.71(+0.17)	0.08	48909.157 <sup>a</sup>	3.80(+0.00)	0.10	52417.496 <sup>f</sup>	4.40(−0.10)	0.10	52417.519 <sup>f</sup>	3.60(−0.30)	0.20
48909.119 <sup>b</sup>	3.40(+0.10)	0.10	51456.050 <sup>e</sup>	3.49(+0.26)	0.07	48910.867 <sup>a</sup>	3.80(+0.00)	0.10	52417.506 <sup>f</sup>	3.90(−0.20)	0.20	53031.748 <sup>f</sup>	2.50(+0.30)	0.20
48910.811 <sup>b</sup>	3.30(+0.00)	0.15	51456.073 <sup>e</sup>	3.42(−0.33)	0.07	48910.886 <sup>a</sup>	3.77(−0.05)	0.08	52417.515 <sup>f</sup>	3.90(+0.00)	0.20	53031.800 <sup>f</sup>	3.50(+0.50)	0.20
48910.962 <sup>b</sup>	3.60(+0.10)	0.15	51456.097 <sup>e</sup>	3.81(+0.20)	0.08	48910.905 <sup>a</sup>	3.46(+0.03)	0.08	52417.523 <sup>f</sup>	3.70(+0.00)	0.20	<b>ν=22 GHz</b>		
48911.114 <sup>b</sup>	4.30(+0.20)	0.15	51456.120 <sup>e</sup>	3.32(+0.06)	0.08	48910.924 <sup>a</sup>	3.73(−0.11)	0.08	52417.531 <sup>f</sup>	3.90(+0.10)	0.20	49803.407 <sup>b</sup>	2.70(+0.10)	0.30
49803.498 <sup>b</sup>	3.00(−0.20)	0.20	51456.144 <sup>e</sup>	3.55(+0.17)	0.08	48911.000 <sup>a</sup>	4.30(+0.10)	0.10	<b>ν=15 GHz</b>			49803.452 <sup>b</sup>	3.50(−0.60)	0.30
49803.647 <sup>b</sup>	3.80(−0.40)	0.20	51458.818 <sup>e</sup>	2.84(−0.01)	0.08	48911.019 <sup>a</sup>	4.00(+0.10)	0.10	48906.841 <sup>a</sup>	4.90(−0.10)	0.30	49803.513 <sup>b</sup>	4.20(+0.50)	0.30
49827.591 <sup>c</sup>	4.50(+0.10)	0.10	51458.841 <sup>e</sup>	3.24(+0.06)	0.07	48911.038 <sup>a</sup>	3.80(+0.00)	0.10	48906.993 <sup>a</sup>	3.40(−0.70)	0.40	49803.557 <sup>b</sup>	3.30(+0.50)	0.20
49833.450 <sup>c</sup>	4.30(−0.10)	0.10	51458.865 <sup>e</sup>	3.59(+0.06)	0.07	48911.057 <sup>a</sup>	3.50(+0.30)	0.10	48907.145 <sup>a</sup>	5.30(−0.40)	0.40	49803.602 <sup>b</sup>	2.90(−0.60)	0.30
49837.398 <sup>c</sup>	3.00(+0.00)	0.10	51458.889 <sup>e</sup>	3.73(−0.07)	0.07	48911.075 <sup>a</sup>	3.80(+0.10)	0.10	48908.836 <sup>a</sup>	3.40(+0.90)	0.40	53031.777 <sup>g</sup>	3.20(+0.60)	0.10
50170.328 <sup>d</sup>	3.30(+0.00)	0.10	51458.920 <sup>e</sup>	3.96(−0.10)	0.08	49803.487 <sup>b</sup>	3.55(+0.00)	0.10	48908.988 <sup>a</sup>	3.20(+0.90)	0.40	53031.828 <sup>g</sup>	4.60(+0.00)	0.10
50170.387 <sup>d</sup>	3.97(−0.04)	0.08	51458.944 <sup>e</sup>	4.05(−0.06)	0.07	49803.636 <sup>b</sup>	3.60(−0.20)	0.10	48909.139 <sup>a</sup>	5.20(+0.50)	0.40	53031.859 <sup>g</sup>	5.30(+0.20)	0.10
50170.446 <sup>d</sup>	4.05(−0.10)	0.08	51458.967 <sup>e</sup>	4.11(−0.16)	0.07	50170.398 <sup>d</sup>	3.84(−0.16)	0.06	48910.831 <sup>a</sup>	3.50(−0.20)	0.40	<b>ν=43 GHz</b>		
50170.506 <sup>d</sup>	3.93(−0.02)	0.07	51458.991 <sup>e</sup>	4.46(−0.11)	0.07	50170.458 <sup>d</sup>	3.50(−0.10)	0.20	48910.982 <sup>a</sup>	4.40(+0.10)	0.40	49803.542 <sup>b</sup>	3.60(−0.20)	0.40
50170.565 <sup>d</sup>	4.28(−0.08)	0.07	51459.019 <sup>e</sup>	4.59(−0.10)	0.06	50170.517 <sup>d</sup>	4.12(−0.13)	0.05	48911.134 <sup>a</sup>	3.00(+1.00)	0.40	49819.488 <sup>c</sup>	3.10(+0.70)	0.80
50170.624 <sup>d</sup>	4.19(−0.02)	0.08	51459.046 <sup>e</sup>	4.95(+0.03)	0.06	50170.576 <sup>d</sup>	4.84(−0.07)	0.05	49803.385 <sup>b</sup>	2.50(+0.10)	0.30	49833.453 <sup>c</sup>	2.00(+0.20)	0.90
50170.684 <sup>d</sup>	3.78(−0.06)	0.08	51459.070 <sup>e</sup>	4.98(−0.06)	0.06	50170.636 <sup>d</sup>	4.69(−0.06)	0.06	49803.430 <sup>b</sup>	3.80(+0.00)	0.25	49837.400 <sup>c</sup>	3.10(+0.90)	0.90
50171.380 <sup>d</sup>	3.14(+0.03)	0.08	51459.094 <sup>e</sup>	4.60(−0.15)	0.07	50170.695 <sup>d</sup>	4.56(−0.14)	0.06	49803.475 <sup>b</sup>	4.30(+0.60)	0.25	53031.763 <sup>g</sup>	2.60(+0.60)	0.20
50171.439 <sup>d</sup>	2.90(+0.02)	0.08	51459.117 <sup>e</sup>	4.97(−0.08)	0.07	50171.391 <sup>d</sup>	3.57(−0.02)	0.06	49803.535 <sup>b</sup>	4.20(−0.10)	0.30	53031.814 <sup>g</sup>	3.00(+0.20)	0.30
50171.499 <sup>d</sup>	3.14(−0.02)	0.07	51459.141 <sup>e</sup>	4.52(+0.04)	0.07	50171.451 <sup>d</sup>	3.56(+0.09)	0.06	49803.580 <sup>b</sup>	3.40(−0.20)	0.25	53031.843 <sup>g</sup>	4.20(+0.60)	0.30
50171.558 <sup>d</sup>	3.55(+0.03)	0.08	51459.163 <sup>e</sup>	3.60(+0.00)	0.10	50171.510 <sup>d</sup>	4.03(−0.03)	0.06	49803.624 <sup>b</sup>	3.20(−0.30)	0.25			
50171.617 <sup>d</sup>	4.00(−0.06)	0.08	51461.935 <sup>e</sup>	4.18(+0.20)	0.06	50171.570 <sup>d</sup>	3.74(−0.10)	0.06	49820.603 <sup>c</sup>	6.00(−0.60)	0.30		</	

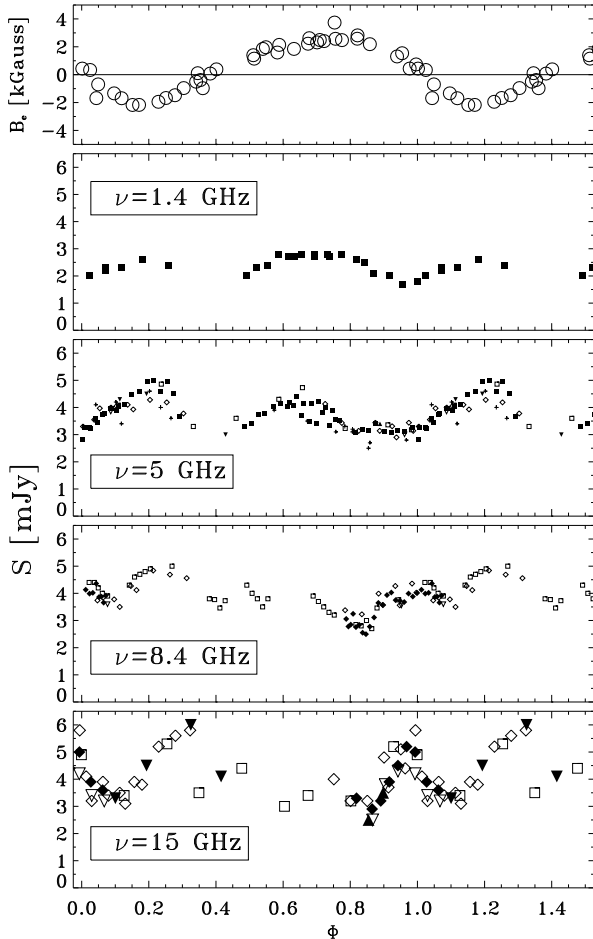


**Figure 2.** VLA measurements of  $\sigma$  Ori E plotted versus the rotation phase  $\Phi$ . Legend of data: AL267 ( $\square$ ), AL348 ( $\nabla$ ), AL346 ( $\blacktriangledown$ ), AL372 ( $\diamond$ ), AT233 ( $\blacksquare$ ), AL568 ( $\blacklozenge$ ) and AL618 ( $\blacktriangle$ ). Literature data at 5 GHz are indicated as (+). Symbol size is equal to the flux error. Top panel reports the literature magnetic field curve.

frequency. It ranges from about 49% (at 1.4 GHz) to about 82% (at 15 GHz) of the median.

With the aim to detect CU Vir type pulses in  $\sigma$  Ori E, we focus our attention in the phase windows where we expect to see them. Those windows are around the rotational phases corresponding to the null of the magnetic field curve. The first null is at  $\Phi \approx 0.9-0.1$ , the second at  $\Phi \approx 0.3-0.5$ , both with a duration  $\Delta\Phi_{\text{null}} \approx 0.2$ . The phase coverage of the radio measurements around the first null is almost continuous in the frequency range 1.4 – 15 GHz, while around the second null there are fewer data. Assuming a pulse extends over a phase window  $\Delta\Phi_{\text{ECM}} \approx 0.05$ , as for the narrowest pulse observed in CU Vir, we estimate that the probability to have missed an ECM pulse in the first null is zero, since the maximum phase gap  $\Delta\Phi_{\text{gap}}$  between contiguous points is smaller than  $\Delta\Phi_{\text{ECM}}$  for all the observed frequencies. On the contrary, around the second null there are several gaps for which  $\Delta\Phi_{\text{gap}} > \Delta\Phi_{\text{ECM}}$ . In this case, we estimate the probability to miss the ECM pulse as  $(\Delta\Phi_{\text{gap}} - \Delta\Phi_{\text{ECM}})/\Delta\Phi_{\text{null}}$ . Considering all the gaps in this phase window, those probabilities are 63%, 25%, 16% and 14%, respectively at 1.5, 5,

8.4 and 15 GHz. For the whole rotational period, instead, we get 13%, 5%, 12% and 15%.

## 4.2 Radio spectrum

The 22 and 43 GHz VLA measurements of  $\sigma$  Ori E do not cover the whole rotational period. However, our 22 and 43 GHz observations are in coincidence with the steep flux increment observed at 15 GHz ( $\Phi \approx 0.95$ ). We can then trace the complete radio spectrum from 1.4 to 43 GHz in the range of phases: 0.9 – 1, when the flux at 15 GHz approximately doubles. To minimize the effect of the lack of simultaneity of higher frequency measurements, we have fixed the phases:  $\Phi = 0.867, 0.910, 0.922, 0.934$  and  $0.998$ , coinciding with the measurements at 43 GHz and with the interpolated value between the two closest in phases 43 GHz observations. Fluxes at the other frequencies have been obtained by fits of the light curves, see Fig. 3, left panels. The five spectra are labelled: (a), (b), (c), (d), and (e) in Fig. 3.

The radio spectrum (a), obtained before the rising phase of the 15 GHz flux, is peaked at intermediate frequencies (5 – 8.4 GHz). The radio spectra ((b), (c) and (d)) just before the 15 GHz maximum are, instead, peaked at higher frequency (15 GHz) and show a steep rise at 43 GHz (Fig. 3, right top panel). At frequencies below 15 GHz the spectral index is positive, with  $\alpha \approx 0.3$  ( $S_\nu \propto \nu^\alpha$ ). The spectrum (e), obtained after the maximum, closely resembles the spectrum (d) (having similar 15 GHz flux level but obtained before the maximum) at the lowest frequencies, whereas at the highest frequencies (22 and 43 GHz) fluxes are decreasing.

## 4.3 Circular polarization

The circularly polarized radio emission shows two extrema of opposite signs (Fig. 4, bottom panels), detected above the  $3\sigma$  detection threshold, associated with the magnetic field extrema (Fig. 1). The degree of polarization enhances as the frequency increases. Positive degree of circular polarization is detected when the north magnetic pole is close to the line of sight and negative in presence of the south pole. When the magnetic poles are close to the direction of the line of sight we observe most of the radially oriented field lines. In this case the gyrosynchrotron mechanism give rise to radio emission partially polarized, respectively right hand for the north pole and left hand for the south pole.

The overall behavior of the circularly polarized radiation from  $\sigma$  Ori E resembles so closely the case of CU Vir at 5, 8.4 and 15 GHz (Leto et al. 2006). This can be considered the typical behavior of the gyrosynchrotron emission from a magnetosphere characterized by a mainly dipolar symmetry.

## 5 EFFECT OF THE MAGNETIC QUADRUPOLE ON THE RADIO EMISSION

### 5.1 Comparison with the 3D model

In order to investigate the radio emission from MCP stars, in Trigilio et al. (2004) we developed a 3D model to compute the gyrosynchrotron emission from a magnetosphere shaped in the framework of the oblique rotator model, that assumes a simple magnetic dipole. Leto et al. (2006) extended the 3D

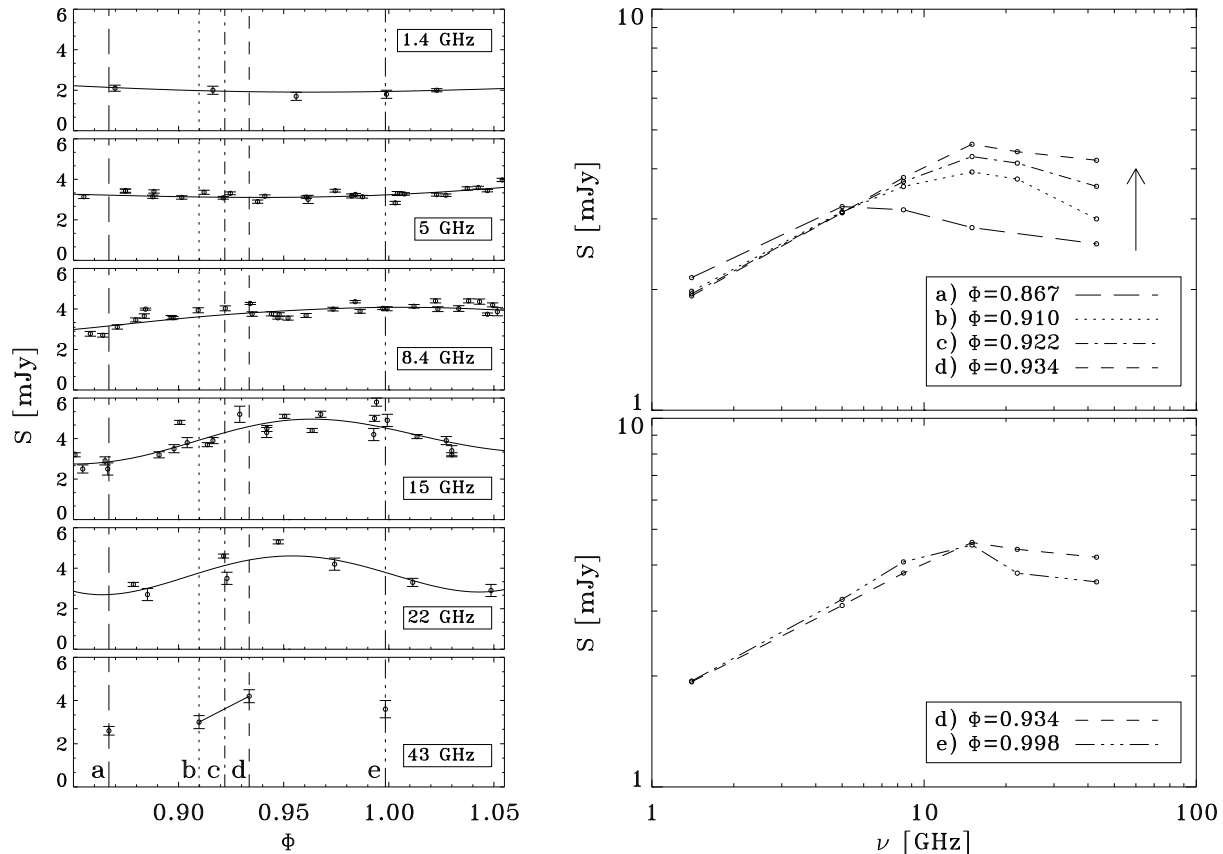


**Figure 3.** Left panels: zoom of the radio light curves at phases where high frequencies data are available; vertical lines (a, b, c, d, e) show the phases where the spectra have been realized. Right panels: radio spectra at phases (a), (b), (c), (d), and (e); rising phase up panel, decay phase down panel.

model to solve the radiation transfer for the circularly polarized emission (Stokes V parameter). Such a 3D modeling has been successfully applied to  $\sigma$  Ori E and HD 37017 by Triglio et al. (2004) and to CU Vir by Leto et al. (2006).

In this model a radiatively driven stellar wind flows along the magnetic field lines. The wind channeled by the magnetic field reaches the magnetic equator. At the Alfvén radius, where the kinetic energy density of the wind exceeds the magnetic one, the stellar wind breaks the magnetic field lines generating current sheets, where particle acceleration occurs. The energetic electrons moving towards the stellar surface emit by gyrosynchrotron mechanism. This thin layer is named middle magnetosphere and it is connected to the annular regions around the magnetic poles at high magnetic latitudes. At lower magnetic latitudes the wind is instead confined in a dead zone (inner magnetosphere), resulting in an accumulation of circumstellar matter whose density decreases outward, in accord with the magnetically confined wind shock model (Babel & Montmerle 1997). This circumstellar material absorbs the continuous gyrosynchrotron radiation, resulting in the observed deep rotational modulation.

Here we adopt the model parameters given by Triglio et al. (2004), used to fit the literature 5 GHz light curve of  $\sigma$  Ori E, to compute the expected radio flux density and fraction of circular polarization ( $\pi_c = S_V/S_I$ ) for all the frequencies. In Fig. 4 we have compared the simula-

tions with the observations. The 1.4 GHz Stokes I variability is reproduced in shape, however slightly overestimating the average flux. As to the highest frequencies, our 3D model fails to reproduce the observed Stokes I variability. On the contrary, Stokes V simulations are in good agreement with the measurements.

Since the source is optically thick, the radiation at different frequencies probes the stellar magnetosphere at different depths, where  $\tau \approx 1$ . Higher frequencies are mainly emitted in the inner regions, where magnetic field is stronger. In particular, inspecting the modeled radio maps of  $\sigma$  Ori E shown by Triglio et al. (2004), the bulk of the 5 GHz gyrosynchrotron emission arise from magnetospheric regions 3 – 8  $R_*$  away from the stellar surface, whereas the 15 GHz originates from inner layers (1 – 5  $R_*$ ).

We conclude that the 3D model reproduces the behavior of the 1.4 and 5 GHz radio emission, coming mainly from regions far from the star, where the dipolar component of the magnetic field dominates. The nearly-dipolar symmetry can be also identified from the behavior of the polarized emission, well reproduced by the model simulations at all the frequencies (Fig. 4, bottom panels). At 8.4 and 15 GHz the model instead fails to reproduce the observed Stokes I modulation, as expected if a non dipolar magnetic field component is present.

In the case of gyrosynchrotron mechanism, the radio emission from a region with almost parallel magnetic field

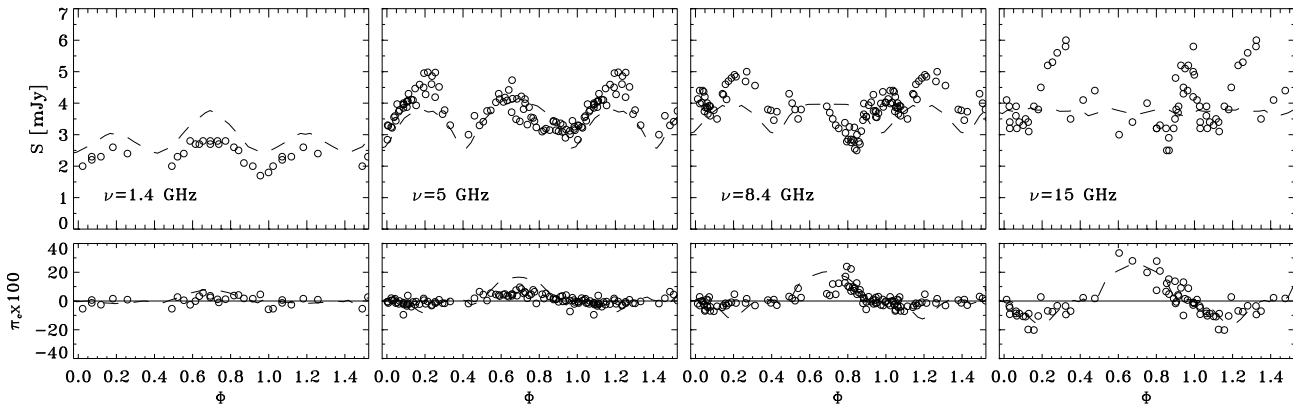


**Figure 4.** Comparison of the observed radio light-curves of  $\sigma$  Ori E and the theoretical curves (dashed line) computed with the 3D model by Triglio et al. (2004).

lines directed toward us (North), or in opposite direction (South), is right-hand (RCP), or left-hand (LCP), circularly polarized; Stokes V, which is the difference between RCP and LCP, is positive, or negative; Stokes I, which is the sum of RCP and LCP is sensitive to both polarizations. In a region with dishomogeneous magnetic field on a small scale, the polarization is, in average, null. When a quadrupolar field is present, we see always regions with antiparallel field lines; Stokes V is always null, while Stokes I depends on the strength of each individual component. In this simple way we can explain the behavior of Stokes V, which well agrees with the dipolar model at any frequency, and of the low frequency Stokes I, arising from regions where only the dipolar field is relevant. The high frequency Stokes I, instead, is sensitive to the quadrupolar component, important in the low magnetosphere. We are supported in such a conclusion from the Stokes I and V variability presented at 5 GHz by HR 5624 (Lim, Drake & Linsky 1996), that is characterized by a multi-polar magnetic field (Landstreet 1990).

The spectra shown in Fig. 3 evidence as the radio flux density at the higher frequencies steeply rise going up to the maximum at phase  $\approx 0.95$ , clearly observed in the 15 GHz light curve. This could be a consequence of strong dishomogeneity in the magnetic field close to the star.

## 5.2 The absence of the cyclotron maser

This work is aimed mainly at searching for CU Vir-like pulses from  $\sigma$  Ori E. In the following we will compute the expected frequency range of the ECM in our target.

The minimum maser frequency observed in CU Vir is 610 MHz (Stevens & George 2010), the maximum is 2.5 GHz. Since the maser frequency is a harmonic of the local gyrofrequency,  $\nu = s \times \nu_B$ , with  $s = 2$ , and assuming a simple dipolar field, for which the magnetic field strength above the pole is given by

$$B_{\text{dip}} = B_p (R_*/R)^3,$$

we can deduce that for CU Vir ( $B_p = 3000$  G) the maser at 610 MHz is generated at  $2 R_*$  above the stellar surface. The shaded area of Fig. 5 defines the frequencies and the corresponding distances associated with the ECM pulses as observed on CU Vir. At the same height, for  $\sigma$  Ori E, with

a polar field strength  $B_p = 6800$  G, the corresponding frequency of emission is 1.4 GHz. Therefore the cyclotron maser emission from  $\sigma$  Ori E, if it does exist, should be observable at frequencies higher than 1.4 GHz. The maximum possible frequency is given by the second harmonic of the gyrofrequency very close to the stellar surface, corresponding to about 38 GHz.

Moreover, a necessary condition for the ECM is that the local plasma frequency must be lower than the local gyrofrequency, i.e.  $\nu_p \ll \nu_B$  (Melrose & Dulk 1982). Since the plasma frequency is given by  $\nu_p = 9 \times 10^{-6} n_e^{1/2}$  GHz, the maser emission near to the magnetic pole is possible only if the local thermal electron number density is less than about  $4 \times 10^{12} \text{ cm}^{-3}$ . In the current model the thin cavity where the maser should originate is the middle magnetosphere above the magnetic pole, where the local plasma is the ionized thermal wind that flows along the magnetic field lines. Following Triglio et al. (2008) and adopting the characteristic values of the wind derived with the 3D model for  $\sigma$  Ori E (Triglio et al. 2004), we estimate that the density of the wind is about  $10^{11} \text{ cm}^{-3}$  near the stellar surface, well below the theoretical quenching limit. As the magnetic field strength decreases going outward, the plasma frequency equates the gyrofrequency at approximately  $7 R_*$  above the surface. Therefore, we can conclude that the condition for generation of the cyclotron maser is satisfied in the middle magnetosphere of  $\sigma$  Ori E.

The radial behavior of the plasma density in the middle and inner magnetosphere, is shown in Fig. 5 for  $\sigma$  Ori E (Triglio et al. 2004) and CU Vir (Leto et al. 2006). As recently observed on CU Vir (Triglio et al. 2011; Lo et al. 2012) the ray path of the ECM, which is polarized in the  $x$ -mode, is refracted by the plasma trapped in the inner magnetosphere, the refractive index is given by  $n_{\text{refr}} \approx \sqrt{1 - \nu_p^2 / 2\nu_B^2}$ , with  $\nu_{\text{ECM}} \approx 2\nu_B$ . Since the conditions of the plasma are quite similar for  $\sigma$  Ori E and CU Vir (Fig. 5), we expect an upwards refraction. In few words the radiation should be deviated, not absorbed.

Despite the light curves in the expected frequency range of the ECM (between 1.4 and 15 GHz) are well sampled, in particular near the rotational phases where we expect to detect it, i.e. in coincidence with at least one null of the magnetic curve (Fig. 2), we do not see any hint of the pulses as

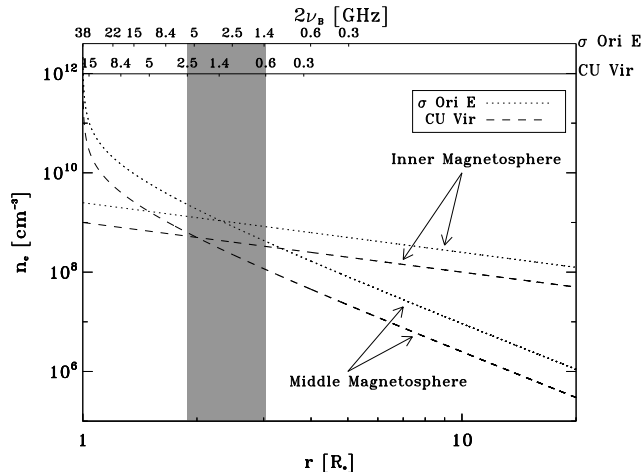


**Figure 5.** Radial dependence of the thermal electron density number inside the “middle” and the “inner” magnetosphere, in the cases of  $\sigma$  Ori E and CU Vir. In the top x-axis the ECM frequencies ( $2\nu_B$ ) for the two stars, are shown, the shaded area identifies the corresponding magnetospheric regions.

observed on CU Vir. Since the frequency of 1.4 and 15 GHz corresponds to the second harmonic of the local gyrofrequency at 2 and 0.4  $R_*$  above the pole respectively, we can conclude that in this region the conditions needed to trigger the cyclotron maser are not fulfilled.

As highlighted in this paper, the magnetic field of  $\sigma$  Ori E is characterized by the presence of a quadrupolar component, whose strength  $B_{\text{quad}}$ , which is prevailing in the stellar surface, decreases faster than the dipolar component ( $B_{\text{quad}} \propto R^{-5}$ ,  $B_{\text{dip}} \propto R^{-3}$ ). Therefore the actual magnetic vector in the low magnetosphere can be quite different from the simple dipolar one. As already discussed, this quadrupolar component significantly affects the gyrosynchrotron emission at high frequency, originating in the deep magnetospheric layers. In a similar way, the quadrupolar component of the magnetic field, stronger than the dipolar one at low altitude, affect the propagation of the electrons moving towards the stellar surface, causing the moving up of the magnetic mirroring point and consequently different interaction with the thermal plasma of the stellar magnetosphere, and possible changing of the ECM conditions. In fact, for a charged particle moving with a pitch angle  $\phi$  in a not uniform magnetic field, its magnetic moment is invariant, i.e.  $\sin^2 \phi / B = \text{constant}$ , leading to magnetic mirroring when the particle moves in a converging magnetic field. Assuming for  $\sigma$  Ori E a simple dipolar field, a non-thermal electron injected with  $\phi_0 \approx 1^\circ$  at the Alfvén radius ( $R_{\text{Alfven}} \approx 15 R_*$ ), where  $B_{\text{Alfven}} \approx 2$  G, will reach the stellar surface with a pitch angle  $\phi \approx 90^\circ$  ( $\sin^2 \phi = \sin^2 \phi_0 \times B_p / B_{\text{Alfven}}$ ). If there is a magnetic quadrupolar component, which is two or three times stronger than the strength of the dipolar field, the same electron is reflected at 0.3 – 0.35  $R_*$  from the surface, and cannot reach the deeper and denser magnetospheric layers; in this case it is reflected back without being absorbed. Only those electrons injected at  $R_{\text{Alfven}}$  with a very small pitch angle ( $\ll 1^\circ$ ) can reach the stellar surface. Accordingly, the fraction of non-thermal electrons that can develop an anisotropic pitch angle distribution is very small, and

then the loss cone angle is already closed when the electrons reach the region where the maser at frequency below 15 GHz should arise. The quadrupole component vanishes 5 – 6  $R_*$  away from the surface and this explain the observed  $\sigma$  Ori E behavior.

## 6 CAN O-TYPE STARS EMIT ECM PULSES?

Hot O-type stars have strong ionized stellar winds and, in few cases, organized magnetic fields (Donati et al. 2002, 2006b), like MCP stars. Such characteristics imply that the magnetic O-type stars may be sources of ECM.

Typically MCP stars have weak winds ( $\dot{M} \approx 10^{-10} - 10^{-9} M_\odot \text{ yr}^{-1}$ ) strongly dominated by the magnetic fields ( $B_p \approx 1-10$  kG), with large co-rotating magnetospheres. The measured magnetic field in the O-type stars is about 1 kG or less (Hubrig et al. 2011) and the mass loss rate is higher than  $10^{-7} M_\odot \text{ yr}^{-1}$ . Since  $R_{\text{Alfven}} \propto B_p^{1/2} / \dot{M}^{1/4}$  (Ud-Doula et al. 2009), the very massive wind and the relatively weak magnetic field locates the Alfvén surface of the known magnetic O-type stars close to the stellar surface ( $< 2 R_*$ ). In the case of single magnetic O-type stars, shocks originating in the wind channeled by the magnetic field can accelerate electrons up to relativistic energy (Van Loo, Runacres & Blomme 2006). These, in turn, could emit at the radio regime by gyrosynchrotron mechanism. On the other hand the O-type stars are characterized by radio emission at centimeter wavelengths mainly ascribed to the thermal free-free emission from the ionized stellar wind, whose typical spectral index is  $\alpha \approx 0.6$  ( $S_\nu \propto \nu^\alpha$ ) (Wright & Barlow 1975). The radio photosphere, at centimeter wavelengths, has a radius of  $\approx 100 R_*$  (Blomme 2011), meaning that the plasma of the wind is optically thick inside and that any non-thermal emission generated within is completely absorbed (Van Loo et al. 2006). The ECM from O-type stars, if any, would suffer from the same absorption effect.

Moreover, for a main sequence magnetic O-type star with stellar radius  $R_* = 7 - 8 R_\odot$ , radiative wind mass loss rate  $\dot{M} = 10^{-6} M_\odot \text{ yr}^{-1}$ , terminal velocity  $v_\infty = 2000$  km  $\text{s}^{-1}$  and dipolar magnetic field with  $B_p = 1000$  G, the condition  $\nu_p > \nu_B$  is valid everywhere. This is a further consideration against the possibility that a magnetic O-type star can emit ECM pulse. Up to now the signatures of non-thermal emission mechanism, flat or negative spectral index and variability, in the O-type stars are observed only in multiple systems, the relativistic electrons origin is thus ascribed to the acceleration in the shocks that take place in the colliding winds far from the stellar surface (Blomme 2011).

In conclusion, the conditions for generation and propagation of the ECM emission are not satisfied for the known magnetic O-type stars. The behavior of the magnetized O-type stars is thus significantly different from the MCP stars (B/A spectral type) in the radio domain. The key to explain when the transition occurs is probably the shaping of the stellar magnetosphere, which depends on mass loss rate, magnetic field strength and rotational period.



## 7 CONCLUSIONS AND OUTLOOK

CU Vir is up to now the only known magnetic chemically peculiar star presenting electron cyclotron maser emission. The characteristics of the MCP star  $\sigma$  Ori E suggest that it should present the same phenomenology of CU Vir at frequencies higher than 1.4 GHz. We have obtained multi frequencies radio observations during the whole the rotation period of  $\sigma$  Ori E, in particular at the phases where the ECM is expected. However, no cyclotron maser emission has been detected in this star.

There are indications that the magnetic field topology of  $\sigma$  Ori E cannot be considered as a simple dipole. The presence of the quadrupole field could inhibit the development of the conditions able to power the cyclotron maser emission. Nevertheless, we cannot rule out the possibility that the ECM could occur at other frequencies not analyzed in this paper, such as the 2.5 GHz, or at phases near the second null of the magnetic curve that are not fully covered.

On the other hand, to better understand the ECM in the wider context of plasma processes it will be extremely interesting to extend such investigation to a bigger sample of MCPs. The average radio luminosity of the MCP stars is about  $10^{16.8 \pm 0.9}$  [ergs s<sup>-1</sup> Hz<sup>-1</sup>] (Drake et al. 1987; Linsky, Drake & Bastian 1992); it has been also shown that the radio luminosity of the MCP stars increases with the effective temperature (Linsky, Drake & Bastian 1992; Leone et al. 1994). The radio interferometers of new generation, like the EVLA or the forthcoming Australian SKA Pathfinder (ASKAP, which will operate at 1.4 GHz), will allow to reach the detection limit of few  $\mu$ Jy in all sky deep surveys. Assuming a threshold of 10  $\mu$ Jy we estimate in about 2000 pc the maximum distance within will be possible to detect the radio emission from the MCPs. Following Renson & Manfroid (2009) we can assume the MCP stars uniformly distributed in space. It is reasonable to expect that the number of radio detections will increase of about an order of magnitude, giving the opportunity to get a larger statistics of the physical conditions of the magnetospheres, like the magnetic field strength and orientation and the thermal plasma density, to correlate with the ECM.

We want to stress here that this class of objects provides the unique possibility to study plasma process in stable magnetic structures, whose topologies are quite often well determined by several independent diagnostics (Bychkov et al. 2005), thus overcoming the variability of the magnetic field that is one of the major problem that prevents an accurate modeling of ECM in very active stars such dMe or close binary systems. On the other side, moving towards earlier spectral types, stronger and denser stellar winds together with a weaker magnetic field should inhibit the onset of the ECM instability. Moreover, as shown for the prototype CU Vir, the observations of persistent coherent pulses of ECM, which act as a clock of the star, in other MCP stars would offer a valuable tool for the angular momentum evolution of the objects belonging to this class.

## ACKNOWLEDGMENTS

We thank the referee for his/her constructive criticism which enabled us to improve this paper.

## REFERENCES

- Abada-Simon M., Lecacheux A., Louarn P., Dulk G.A., Belkora L., Bookbinder J.A., Rosolen C., 1994, *A&A*, 288, 219
- Abada-Simon M., Lecacheux A., Aubier M., Bookbinder J.A., 1997, *A&A*, 321, 841
- Babcock H.W., 1949, *Observatory*, 69, 191
- Babel J., Montmerle T., 1997, *A&A*, 323, 121
- Berger E., et al., 2001, *Nat*, 410, 338
- Blomme R., 2011, *BSRSL*, 80, 67
- Bohlender D.A., Landstreet J.D., Brown D.N., Thompson I.B., 1987, *ApJ*, 323, 325
- Burgasser A.J., Putman M.E., 2005, *ApJ*, 626, 486
- Bychkov V.D., Bychkova L.V., Madej J., 2005, *A&A*, 430, 1143
- Catalano F.A., Renson P., 1984, *A&AS*, 55, 371
- Catalano F.A., Renson P., 1988, *A&AS*, 72, 1
- Catalano F.A., Renson P., Leone F., 1991, *A&AS*, 87, 59
- Catalano F.A., Kroll R., Leone F., 1991, *A&A*, 248, 179
- Catalano F.A., Renson P., Leone F., 1993, *A&AS*, 98, 269
- Donati J.-F., Babel J., Harries T.J., Howarth I.D., Petit P., Semel M., 2002, *MNRAS*, 333, 55
- Donati J.-F., Forveille T., Collier Cameron A., Barnes, J.R., Delfosse X., Jardine M.M., Valenti J.A., 2006a, *Sci*, 311, 633
- Donati J.-F., Howarth I.D., Bouret J.-C., Petit P., Catala C., Landstreet J., 2006b, *MNRAS*, 365, L6
- Donati J.-F., et al., 2008, *MNRAS*, 390, 545
- Drake S.A., Abbot D.C., Bastian T.S., Biegging J.H., Churchwell E., Dulk G., Linsky J.L., 1987, *ApJ*, 322, 902
- ESA, 1997, *The Hipparcos and Tycho Catalogues*, ESA SP-1200
- Groote D., Hunger K., 1982, *A&A*, 116, 64
- Hallinan G., Antonova A., Doyle J.G., Bourke S., Brisken W.F., Golden A., 2006, *ApJ*, 653, 690
- Hallinan G., et al., 2007, *ApJ*, 663, L25
- Hallinan G., Antonova A., Doyle J.G., Bourke S., Lane C., Golden A., 2008, *ApJ*, 684, 644
- Hubrig S., et al., 2011, *A&A*, 528, 151
- Hunger K., Heber U., Groote D., 1989, *A&A*, 224, 57
- Landolfi M., Bagnulo S., Landi Degl'Innocenti M., 1998, *A&A*, 338, 111
- Landstreet J.D., Borra E.F., 1978, *ApJ*, 224, L5
- Landstreet J.D., 1990, *ApJ*, 352, L5
- Lang K.R., Bookbinder J., Golub L., Davis M.M., 1983, *ApJ*, 272, L15
- Lang K.R., Willson R.F., 1988, *ApJ*, 326, 300
- Leone F., 1991, *A&A*, 252, 198
- Leone F., Catalano F.A., Catanzaro G., 2000, *A&A*, 355, 315
- Leone F., Umana G., 1993, *A&A*, 268, 667
- Leone F., Trigilio C., Umana G., 1994, *A&A*, 283, 908
- Leone F., Bohlender D.A., Bolton C.T., Buemi C., Catanzaro G., Hill G.M., Stift M.J., 2010, *MNRAS*, 401, 2739
- Leto P., Trigilio C., Buemi C.S., Umana G., Leone F., 2006, *A&A*, 458, 831
- Lim J., Drake S.A., Linsky J.L., 1996, *ASPC*, 93, 324
- Linsky J.L., Drake S.A., Bastian S.A., 1992, *ApJ*, 393, 341
- Lo K.K., et al., 2012, *MNRAS*.tmp.2564
- Melrose D.B., Dulk G.A., 1982, *ApJ*, 259, 844
- Morin J., et al., 2008a, *MNRAS*, 384, 77

- Morin J., et al., 2008b, MNRAS, 390, 567  
Mutel R.L., Christopher I.W., Pickett J.S., 2008, GeoRL, 35, L07104.  
Oksala M.E., Wade G.A., Townsend R.H.D., Kochukhov O., Owocki S.P., 2011, Proc. IAU Symp. 272, Active OB stars: structure, evolution, mass loss, and critical limits, p. 124  
Osten R.A., et al., 2004, ApJS, 153, 317  
Ravi V., Hobbs G., Wickramasinghe D., Champion D.J., Keith M., 2010, MNRAS, 408, L99  
Renson P., Manfroid J., 2009, A&A, 498, 961  
Shore N.S., Brown N.B., 1990, ApJ, 365, 665  
Slee O.B., Haynes R.F., Wright A.E., 1984, MNRAS, 208, 865  
Smith M.A., Groote D., 2001, A&A, 372, 208  
Schnerr R.S., Rygl K.L.J., van der Horst A.J., Oosterloo T.A., Miller-Jones J.C.A., Henrichs H.F., Spoelstra T.A.Th., Foley A.R., 2007, A&A, 470, 1105  
Stevens I.R., George S.J., 2010, ASPC, 422, 135  
Stibbs D.W.N., 1950, MNRAS, 110, 395  
Townsend R.H.D., Oksala M.E., Cohen D.H., Owocki S.P., ud-Doula A., 2010, ApJ, 714, L318  
Treumann R.A., 2006, A&ARv, 13, 229  
Trigilio C., Leto P., Leone F., Umana G., Buemi C., 2000, A&A, 362, 281  
Trigilio C., Leto P., Umana G., Leone F., Buemi C.S., 2004, A&A, 418, 593  
Trigilio C., Leto P., Umana G., Buemi C.S., Leone F., 2008, MNRAS, 384, 1437  
Trigilio C., Leto P., Umana G., Buemi C.S., Leone F., 2011, ApJ, 739, L10  
Ud-Doula A., Owocki S.P., Townsend R.H.D., 2009, MNRAS, 392, 1022  
Van Loo S., Runacres M.C., Blomme R., 2006, A&A, 452, 1011  
Willson R.F., 1985, SoPh, 96, 199  
Wingle R.M., Dulk G.A., 1986, ApJ, 310, 432  
Wright, A.E., Barlow M.J. 1975, MNRAS, 170, 41